Calibration of the liquid argon ionization response to low energy electronic and nuclear recoils with DarkSide-50

P. Agnes et al. (DarkSide Collaboration)

Calibration of the liquid argon ionization response to low energy electronic and nuclear recoils with DarkSide-50

P. Agnes,[1] I.F.M. Albuquerque,[2] T. Alexander,[3] A.K. Alton,[4] M. Ave,[2] H.O. Back,[3] G. Batignani,[5,6] K. Biery,[7] V. Bocci,[8] W.M. Bonivento,[9] B. Bottino,[10,11] S. Bussino,[12,13] M. Cadeddu,[9] M. Cadoni,[14,9] F. Calaprice,[15] A. Caminata,[11] N. Canci,[16] M. Caravati,[9] M. Cariello,[11] M. Carlini,[16,17] M. Carpinelli,[18,19] S. Catalanotti,[20,21] V. Cataudella,[20,21] P. Cavalcante,[22,16] S. Cavuoti,[20,21] A. Chepurnov,[23] C. Cicalò,[9] A.G. Cocco,[21] G. Covone,[20,21] D. D'Angelo,[24,25] S. Davini,[11] A. De Candia,[20,21] S. De Cecco,[8,26] G. De Filippis,[20,21] G. De Rosa,[20,21] A.V. Derbin,[27] A. Devoto,[14,9] M. D'Incecco,[16] C. Dionisi,[8,26] F. Dordei,[9] M. Downing,[28] D. D'Urso,[18,19] G. Fiorillo,[20,21] D. Franco,[29] F. Gabriele,[9] C. Galbiati,[15,17,16] C. Ghiano,[16] C. Giganti,[30] G.K. Giovanetti,[15] O. Gorchakov,[31,*] A.M. Goretti,[16] A. Grobov,[32,33] M. Gromov,[23,31] M. Guan,[34] Y. Guardincerri,[7,*] M. Gulino,[35,19] B.R. Hackett,[3] K. Herner,[7] B. Hosseini,[9] F. Hubaut,[36] E.V. Hungerford,[1] An. Ianni,[15,16] V. Ippolito,[8] K. Keeter,[37] C.L. Kendziora,[7] I. Kochanek,[16] D. Korablev,[31] G. Korga,[1,16] A. Kubankin,[38] M. Kuss,[5] M. La Commara,[20,21] M. Lai,[14,9] X. Li,[15] M. Lissia,[9] G. Longo,[20,21] I.N. Machulin,[32,33] L.P. Mapelli,[39] S.M. Mari,[12,13] J. Maricic,[40] C.J. Martoff,[41] A. Messina,[8,26] P.D. Meyers,[15] R. Milincic,[40] M. Morrocchi,[5,6] X. Mougeot,[42] V.N. Muratova,[27] P. Musico,[11] A. Navrer Agasson,[30] A.O. Nozdrina,[32,33] A. Oleinik,[38] F. Ortica,[43,44] L. Pagani,[45] M. Pallavicini,[10,11] L. Pandola,[19] E. Pantic,[45] E. Paoloni,[5,6] K. Pelczar,[16,46] N. Pelliccia,[43,44] E. Picciau,[14,9] A. Pocar,[28] S. Pordes,[7] S.S. Poudel,[1] P. Pralavorio,[36] F. Ragusa,[24,25] M. Razeti,[9] A. Razeto,[16] A.L. Renshaw,[1] M. Rescigno,[8] J. Rode,[30,29] A. Romani,[43,44] D. Sablone,[15,16] O. Samoylov,[31] W. Sands,[15] S. Sanfilippo,[13,12] C. Savarese,[17,16,15] B. Schlitzer,[45] D.A. Semenov,[27] A. Shchagin,[38] A. Sheshukov,[31] M.D. Skorokhvatov,[32,33] O. Smirnov,[31] A. Sotnikov,[31] S. Stracka,[5] Y. Suvorov,[20,21,32] R. Tartaglia,[16] G. Testera,[11] A. Tonazzo,[29] E.V. Unzhakov,[27] A. Vishneva,[31] R.B. Vogelaar,[22] M. Wada,[15,47] H. Wang,[39] Y. Wang,[39,34] S. Westerdale,[15,9] M.M. Wojcik,[46] X. Xiao,[39] C. Yang,[34] and G. Zuzel[46]

(The DarkSide Collaboration)

[1] *Department of Physics, University of Houston, Houston, TX 77204, USA*
[2] *Instituto de Física, Universidade de São Paulo, São Paulo 05508-090, Brazil*
[3] *Pacific Northwest National Laboratory, Richland, WA 99352, USA*
[4] *Physics Department, Augustana University, Sioux Falls, SD 57197, USA*
[5] *INFN Pisa, Pisa 56127, Italy*
[6] *Physics Department, Università degli Studi di Pisa, Pisa 56127, Italy*
[7] *Fermi National Accelerator Laboratory, Batavia, IL 60510, USA*
[8] *INFN Sezione di Roma, Roma 00185, Italy*
[9] *INFN Cagliari, Cagliari 09042, Italy*
[10] *Physics Department, Università degli Studi di Genova, Genova 16146, Italy*
[11] *INFN Genova, Genova 16146, Italy*
[12] *INFN Roma Tre, Roma 00146, Italy*
[13] *Mathematics and Physics Department, Università degli Studi Roma Tre, Roma 00146, Italy*
[14] *Physics Department, Università degli Studi di Cagliari, Cagliari 09042, Italy*
[15] *Physics Department, Princeton University, Princeton, NJ 08544, USA*
[16] *INFN Laboratori Nazionali del Gran Sasso, Assergi (AQ) 67100, Italy*
[17] *Gran Sasso Science Institute, L'Aquila 67100, Italy*
[18] *Chemistry and Pharmacy Department, Università degli Studi di Sassari, Sassari 07100, Italy*
[19] *INFN Laboratori Nazionali del Sud, Catania 95123, Italy*
[20] *Physics Department, Università degli Studi "Federico II" di Napoli, Napoli 80126, Italy*
[21] *INFN Napoli, Napoli 80126, Italy*
[22] *Virginia Tech, Blacksburg, VA 24061, USA*
[23] *Skobeltsyn Institute of Nuclear Physics, Lomonosov Moscow State University, Moscow 119234, Russia*
[24] *Physics Department, Università degli Studi di Milano, Milano 20133, Italy*
[25] *INFN Milano, Milano 20133, Italy*
[26] *Physics Department, Sapienza Università di Roma, Roma 00185, Italy*
[27] *Saint Petersburg Nuclear Physics Institute, Gatchina 188350, Russia*
[28] *Amherst Center for Fundamental Interactions and Physics Department, University of Massachusetts, Amherst, MA 01003, USA*
[29] *APC, Université de Paris, CNRS, Astroparticule et Cosmologie, Paris F-75013, France*
[30] *LPNHE, CNRS/IN2P3, Sorbonne Université, Université Paris Diderot, Paris 75252, France*
[31] *Joint Institute for Nuclear Research, Dubna 141980, Russia*
[32] *National Research Centre Kurchatov Institute, Moscow 123182, Russia*
[33] *National Research Nuclear University MEPhI, Moscow 115409, Russia*
[34] *Institute of High Energy Physics, Beijing 100049, China*
[35] *Engineering and Architecture Faculty, Università di Enna Kore, Enna 94100, Italy*

[36] *Centre de Physique des Particules de Marseille, Aix Marseille Univ, CNRS/IN2P3, CPPM, Marseille, France*
[37] *School of Natural Sciences, Black Hills State University, Spearfish, SD 57799, USA*
[38] *Radiation Physics Laboratory, Belgorod National Research University, Belgorod 308007, Russia*
[39] *Physics and Astronomy Department, University of California, Los Angeles, CA 90095, USA*
[40] *Department of Physics and Astronomy, University of Hawai'i, Honolulu, HI 96822, USA*
[41] *Physics Department, Temple University, Philadelphia, PA 19122, USA*
[42] *Université Paris-Saclay, CEA, List, Laboratoire National Henri Becquerel (LNE-LNHB), F-91120 Palaiseau, France*
[43] *Chemistry, Biology and Biotechnology Department, Università degli Studi di Perugia, Perugia 06123, Italy*
[44] *INFN Perugia, Perugia 06123, Italy*
[45] *Department of Physics, University of California, Davis, CA 95616, USA*
[46] *M. Smoluchowski Institute of Physics, Jagiellonian University, 30-348 Krakow, Poland*
[47] *AstroCeNT, Nicolaus Copernicus Astronomical Center, 00-614 Warsaw, Poland*

DarkSide-50 has demonstrated the high potential of dual-phase liquid argon time projection chambers in exploring interactions of WIMPs in the GeV/c^2 mass range. The technique, based on the detection of the ionization signal amplified via electroluminescence in the gas phase, allows to explore recoil energies down to the sub-keV range. We report here on the DarkSide-50 measurement of the ionization yield of electronic recoils down to ∼180 eV$_{er}$, exploiting ^{37}Ar and ^{39}Ar decays, and extrapolated to a few ionization electrons with the Thomas-Imel box model. Moreover, we present a model-dependent determination of the ionization response to nuclear recoils down to ∼500 eV$_{nr}$, the lowest ever achieved in liquid argon, using *in situ* neutron calibration sources and external datasets from neutron beam experiments.

I. INTRODUCTION

Dual-phase noble liquid time projection chambers (TPCs) have yielded, for more than a decade, ever increasing world leading sensitivity for the search for Weakly Interacting Massive Particles (WIMPs) with mass greater than 10 GeV/c^2 [1–5]. In recent years, the dual-phase technology has been extended to search for "light" dark matter candidates using the ionization component only, which allows to explore the sub-keV energy range. Experiments like XENON1T with a liquid xenon target [6, 7] and DarkSide-50 with liquid argon (LAr) [8, 9] have set the best limits on WIMP-nucleus interactions for M$_\chi$>1.8 GeV/c^2 (M$_\chi$>0.1 GeV/c^2 exploiting the Migdal effect), WIMP-electron scattering for M$_\chi$>30 MeV/c^2, and absorption of dark photons and axion-like particles for M$_\chi$≳0.2 keV/c^2. This was possible thanks to the intrinsic radiopurity, and high ionization yield and resolution, allowing for detection of single electrons, of noble liquids.

Unlike xenon, for which there exists a rich set of measurements that characterize its ionization response in the keV range (see, for instance. Refs [10–14]), the argon response is almost unexplored. In spite of the smaller cross section of WIMP scattering on argon compared to xenon, due to the lower atomic number, interactions in argon produce more energetic recoils, with a higher probability of being detected above the threshold. The potential of dual-phase LAr TPC technology in direct dark matter search can therefore be significantly enhanced through a better understanding of the ionization response, especially in the sub-keV region. This represents the focus of this paper, through the measurement of the ionization

response to electronic (ER) and nuclear (NR) recoils with DarkSide-50, using β-decay sources intrinsic to LAr, *i.e.* ^{37}Ar and ^{39}Ar, and neutron sources located just outside the TPC, specifically ^{241}Am-^{13}C and ^{241}Am-^{11}Be. In addition, external datasets from beam test experiments are included in the analysis to better constrain the NR ionization response. This approach, already adopted in the so-called DarkSide-50 *low-mass* analyses published in 2018 [8, 9], is presented in this paper in detail after being highly refined and improved.

Such calibrations not only have the potential to improve current limits with DarkSide-50, but also provide a basis for future detectors specifically designed to search for light dark matter candidates with LAr.

II. THE DARKSIDE-50 EXPERIMENT

The DarkSide-50 experiment is located in Hall C of the Gran Sasso National Laboratory (LNGS) in Italy. The TPC has a cylindrical active LAr target of ∼46 kg The lateral walls are made of polytetrafluoroethylene (PTFE), surrounded by field shaping copper rings. Two arrays of 19 3-in diameter photomultiplier tubes (PMTs) are located on both ends behind the transparent anode and cathode respectively. They observe light signals from both primary scintillation (S1) and electroluminescence (S2) from ionization electrons, extracted in the gas phase, after being drifted with a 200 V/cm field in liquid. The extraction efficiency is estimated >99.9% at the extraction field of 2.8 kV/cm. The PTFE and the fused silica windows at the top and bottom of the cylinder are coated with tetraphenyl butadiene (TPB), a wavelength shifter, that absorbs the 128 nm photons emission and re-emits softer photons with a peak wavelength at 420 nm.

The TPC was first operated, between 2013 and 2014, with atmospheric argon, and then until 2019, with low-

───────

* Deceased.

radioactivity argon extracted from deep underground, naturally shielded against cosmogenic isotope production. For a more detailed description of the TPC, see ref. [15, 16].

The TPC is surrounded by a hermetic neutron veto, a 4 m diameter stainless steel sphere filled with 30 t of liquid scintillator, loaded with trimethyl borate molecule (TMB) at 5% mass fraction. 110 8-inch PMTs are mounted on the inner surface of the sphere to detect the scintillation light. Neutrons are mostly captured by ^{10}B present in TMB via the ^{10}B(n, α)^{7}Li* and ^{10}B(n, α)^{7}Li reactions, with a mean capture time of $\sim$22 μs [17], thanks to the large ^{10}B cross section for thermal neutron. The first reaction, with 93.6% branching ratio, is also responsible for the emission of a characteristic 478 keV γ from the ^{7}Li* de-excitation, efficiently detected thanks to the relatively high light yield of the scintillator ($\sim$530 pe/MeV).

The neutron veto is in turn immersed in 1000 t of ultrapure water, instrumented as a Cherenkov veto against cosmic muons, and passive shield against external background. See ref. [17] for more details on the veto system.

III. DETECTOR RESPONSE MODEL

The DarkSide-50 ionization signals are affected by instrumental effects, like the smearing induced by gas-phase electroluminescence and by the PMT charge response. The measured S2 yield (g_2), defined as the mean number of photoelectrons per ionization electron extracted in the gas pocket, and the associated relative resolution are 23$\pm$1 pe/e$^-$ and $\sim$27%, respectively, for events localized beneath the central PMT [8]. An additional instrumental effect is related to the electron lifetime, *i.e.* the survival time of an electron to the capture from impurities in LAr along the drift. This was measured to be about 10 ms, almost 30 times longer than the maximum drift time in the TPC (376 μs [5]). The distortion of the ionization signal induced by the electron lifetime is therefore limited to a few percent.

The dominant instrumental effect is the dependence of the S2 response on the event radial position on the *xy*-plane, orthogonal to the electric field. The S2 response yields a factor of $\sim$4 difference between the centre and the edges of the TPC. This has been assessed using the 41.5 keV line from the ^{83m}Kr gas source injected into the active mass, and applying the position reconstruction algorithm [18], which provides a sub-cm-level resolution. Such a distortion may be due either to a non-uniformity of the TPB thickness, on the top fused-silica window, which would produce non-uniform conversion of VUV scintillation, or to the sagging of the window itself, resulting in a varying thickness of the gas pocket, and, in turn, of the number of electron-luminescence photons produced.

S2 pulses can be corrected using the radial-dependent efficiency measured with ^{83m}Kr data. However, the energy range of interest for the *low-mass* analysis extends down to $\sim$100 eV, where the reconstruction algorithm is inefficient because of the low number of S2 photoelectrons. The analysis published in 2018 [8] overcame this issue by exploiting a channel-based correction that defines the event position as that of the top-plane PMT (Ch_{max}), which observes the largest fraction of photoelectrons. The position correction based on this definition is rather coarse, because it does not take the finite size (3-inches) of the DarkSide-50 PMTs into account.

To improve the accuracy of the measurement of the intrinsic LAr response to ionization signals, all effects mentioned in this section have been incorporated into a Monte Carlo simulation. This approach has been validated on a sample of ^{37}Ar decays, naturally present in LAr. This cosmogenic background decays via a single electron capture transition, ground-state to ground-state, with a half-life of 35.01 (2) d [19].

The dominant ^{37}Ar decay branches are from the electron capture on K (2.83 keV) and L1 (0.277 keV) atomic shells, with branching ratios of $\sim$90.4% and $\sim$8.4%, respectively, determined with the `BetaShape` code [20, 21] using the latest recommended Q-value of 813.87 (20) keV [22]. The emitted cascades of electrons, X-rays, and UV photons are evaluated with the `RELAX` software [23], based on the latest `EADL2017` library of atomic transition data [24]. `RELAX` calculates atomic relaxation spectra of UV photons, X-rays and Auger electrons, hereafter referred to as "primaries", due to bound-state-to-bound-state transitions for a single initial vacancy in the different sub-shells. From the atomic transition probabilities, a deterministic step-by-step propagation of the vacancies was made up to the valence shell and to the neutralization. Atomic configuration has been accounted for, rejecting transitions that would require more electrons in a sub-shell than those actually present. It should be underlined that the only information available in the `EADL2017` library is for a single atomic vacancy. In principle, each additional vacancy due to an Auger transition would require a complete recalculation of the atomic energies, wave functions and transition probabilities, which is not considered in this work.

The relaxation paths estimated by `RELAX` are 5213 and 72 for the K and L1 shells, respectively. Each contribution is determined per initial vacancy and weighted by the corresponding capture probability. The average energies of Auger electrons, UV photons and X-rays grouped by shell, are quoted in Table I. We can assume that the primary particle is almost always an electron, either because directly emitted or because extracted by X-rays or UV photons via photoelectric effect. The K- and L1-shells emit, on average 3.9 and 2.8 primaries, respectively, neglecting UV photons with energy not sufficient to photoionize an ^{40}Ar atom. To evaluate the ionization yield, the mean number of primaries will be subtracted from the number of detected electrons, as primaries are also drifted and extracted in the gas pocket and contribute to the S2 signal.

	K–shell EC		L1–shell EC	
Branching Ratio	90.4%		8.4%	
Total Released Energy	2829		277	
Mean number of primaries[a]	3.9		2.8	
	⟨N⟩	⟨E⟩	⟨N⟩	⟨E⟩
K Auger electrons	0.905	2414		
K X-rays	0.095	2634		
L Auger electrons	1.77	179	0.9995	179
L X-rays	8E-4	188	0.0005	207
M Auger electrons	0.35	51	0.96	51
UV photons (E>16 eV)	0.77	25	0.86	25
Undetectable via ionization	3.26	13	2.10	13

[a] Excluding undetectable via ionization

TABLE I. Average numbers ($\langle N \rangle$) and energies ($\langle E \rangle$) of primaries (electrons, X-rays and UV photons) emitted in electron capture-induced cascades on ^{37}Ar K and L1 shells as determined using `RELAX` [23] and the `EADL2017` library [24]. The capture probabilities were evaluated with `BetaShape` [20, 21]. All energies are expressed in eV.
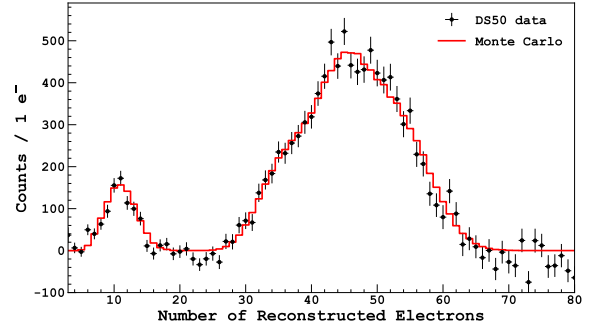

FIG. 1. Comparison between the best fitted simulated spectrum and ^{37}Ar data as a function of the reconstructed number of electrons. The free parameters in the model are the mean number of ionization electrons induced by the ^{37}Ar L1- and K-shell electrons, and the Fano factor.

The two lines from K and L1 electron capture are observed in the DarkSide-50 data by subtracting the latest ~500 days of the underground argon campaign dataset (from 2015 to 2018), where ^{37}Ar is almost entirely decayed, from the first ~100 days, normalizing the two samples by their livetimes. The subtracted spectrum is fitted with simulated spectra, generated by independently varying the average number of detected electrons (N_e) for each of the two ^{37}Ar lines. Events are simulated with a uniform spatial distribution in the TPC. The intrinsic fluctuations induced by the number of emitted particles and by the LAr ionization response to ERs are modelled with an empirical fudge factor implemented as a Fano factor [25]. In the Monte Carlo, a fraction of electrons is suppressed according to the electron lifetime. The surviving free electrons are extracted in the gas pocket with 100% efficiency, and converted into S2 photoelectrons with g_2 that varies depending on the xy-position of the event, according to relative efficiency derived with the ^{83m}Kr calibration source.

The fit is performed with a χ^2 analysis, where the free parameters are the numbers of extracted electrons induced by the two ^{37}Ar lines and the Fano factor. It is worth mentioning that no additional correction is applied to the resolution model. The shoulder-like structure observed at ~35 e^- in Figure 1 originates from the non-uniform radial response of the detector and is well reproduced by the Monte Carlo starting from input parameters only.

The resulting numbers of electrons are 12.0±0.1($stat.$)±0.5($syst.$) and 48.2±0.2($stat.$)±2.1($syst.$) for the ^{37}Ar L1– and K–shell, respectively. The systematic errors are calculated by propagating the uncertainty on the g_2 value. The best-fitted simulated spectrum is shown in Figure 1 together with data, as a function of the reconstructed number of electrons. The fit returns a reduced χ^2 of 82.4 / 64.

The ratio between the measured amplitudes of the two lines, equal to 0.10±0.01, is in excellent agreement with ~0.093, the expected value determined with `BetaShape`, and with measured values in literature (0.103±0.003 [26], 0.102±0.004 [27], 0.098±0.003 [28]).

The fitted Fano factor, 0.10±0.03, is compatible with predictions on the LAr ionization fluctuation from the Shockley (0.107) and the Alkhazov (0.116) models [29]. This result suggests that intrinsic fluctuations of the number of particles emitted in atomic cascades are negligible compared to the ionization fluctuation.

As already mentioned, in order to extract the number of ionization electrons from the two lines, the number of emitted primaries in the atomic cascades must be subtracted from the number of detected electrons. In the L1–shell cascade, the mean number of primaries is 2.8. The 25 eV UV has high probability of extracting an electron by photoionization, but with insufficient energy to induce additional ionization electrons.

The 51 eV M-shell electron is sufficiently energetic to ionize up to two atoms. The Thomas-Imel model, discussed in the following section, predicts a suppressed ion-electron recombination probability at such low ionization densities [30], a finding confirmed by numerical simulations [31]. Yet the energy lost to excitations is unknown at such low energies. Therefore because of uncertainties on the ionization mechanism, we conservatively assume that the 51 eV line contributes with 1±1 ionization electrons to the L1-shell cascade. In addition, we assume negligible interactions between the 51 eV and the L-shell 179 eV electron-ion clouds because of their low ionization density. The resulting number of ionization electron at 179 eV is 8.2±1.3, where the uncertainty takes into account both statistical and systematic errors, corresponding to a ionization yield of 45.7±7.0 e^-/keV$_{er}$.

Unlike the L1–shell, the superposition of ~3 ion-electron clouds from K–shell electrons of 2414 eV (or 2634 eV X-rays) and 179 eV (1.8 multiplicity) cannot be ne-

glected. However, the lack of a model able to describe the complex event topology does not allow to estimate the overall recombination effect. For this reason, we do not include data from ^{37}Ar K–shell in the analysis, discussed in the following section, for the determination of the ER ionization yield.

IV. ELECTRONIC RECOIL IONIZATION YIELD

The calibration of the ER energy scale relies on ^{37}Ar data, discussed in the previous section, and on the cosmogenic ^{39}Ar β^--decay sample from the 2013-2014 atmospheric argon (AAr) campaign [15], acquired with the same drift field of 200 V/cm. In AAr, ^{39}Ar has a specific activity of $\sim$1 Bq/kg [15], and dominates the event rate. To suppress the "external" background from radioactivity in detector materials surrounding the active mass, events are selected within a central cylinder with 2 cm radius and 21.6 cm height, 16.8 cm far from the lateral walls and 7 cm from the top and bottom of the TPC. The very narrow cut in radius selects events corresponding to the innermost area of the central PMT only, minimizing the non-uniformity of the detector response. To further remove residual external contamination, events with more than one S2 pulse are rejected. These are multiple scatter events, and not compatible with the topology of the ^{39}Ar β-decay signature.

The kinetic energy of each event is reconstructed exploiting the full anti-correlation between the S1 and S2 signals, through the so-called "rotated" energy variable

$$E_{er} = w \left(\frac{S1}{g_1} + \frac{S2}{g_2} \right), \tag{1}$$

where w=19.5$\pm$1.0 eV [32] is the average energy required to produce a quantum (excitation or ionization) and g_1 the S1 collection efficiency (0.16$\pm$0.01 [18]). The number of ionization electrons escaping the ion-electron recombination process, $N_{i.e.}$, is calculated for each event of the ^{39}Ar sample as

$$N_{i.e.} = \frac{S_2}{g_2} - 1, \tag{2}$$

which accounts for the subtraction of the primary electron from the β-decay. The mean value of the ER ionization yield, Q_y^{ER}, is estimated using eqs. 1 and 2 for each 0.2–keV$_{er}$ bin. A lower threshold of E_{er}>1.7 keV is applied to guarantee 100% efficiency in the identification of the S1 pulse. The uncertainty is dominated by the systematics from the g_2 parameter.

The ionization yield per unit of ER energy from ^{37}Ar and ^{39}Ar data is defined as

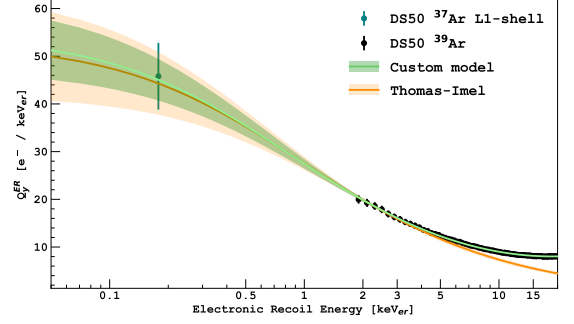$$Q_y^{ER} = \frac{N_{i.e.}}{E_{er}} = \frac{(1-r)N_i}{E_{er}}, \tag{3}$$

FIG. 2. Fit of the ER ionization yield, measured from AAr (black) and ^{37}Ar (teal) data with a drift field of 200 V/cm, with the Thomas-Imel box model up to 3 keV$_{er}$ (eq. 4), and with the custom model from eq. 6, which extends the Thomas-Imel model up to 20 keV$_{er}$. The model bands correspond to 1σ, also accounting for the correlation from the g_2 systematics, which dominates the experimental uncertainties.

where N_i is the number of produced electron-ion pairs. The electron recombination probability (r) is predicted at low energies, $\mathcal{O}$(keV$_{er}$), by the Thomas-Imel box model [30],

$$1 - r = \frac{1}{\gamma N_i} \ln(1 + \gamma N_i), \tag{4}$$

where γ is a free parameter describing the recombination of the initial electron-ion pairs contained in a box and immersed in an electric field. This model has proven to work well in noble liquids for spatially short tracks [33], in the $\mathcal{O}$(keV$_{er}$) range for ERs. In this range, Eq. 3 can be parametrized as

$$Q_y^{ER} = \frac{1}{\gamma} \frac{\ln(1 + \gamma \rho E_{er})}{E_{er}}, \tag{5}$$

with ρ=N_i/E_{er} and γ the free parameters of the model. γ can be expressed as C_{box}/F, where F is the drift field (200 V/cm) and C_{box} depends on the mean ionization electron velocity and on the size of the ideal box containing the electron-ion cloud. In this parameterization, we assume the approximation of a constant excitation-to-ionization ratio, which implies that N_i is proportional to the deposited energy [18]. The impact of this approximation is discussed at the end of this section.

^{39}Ar data, together with the ^{37}Ar calibration line, are fitted with Eq. 5 up to 3 keV$_{er}$. As shown in Figure 2, the Thomas-Imel box model is in good agreement with ^{37}Ar and ^{39}Ar data points with E$_{er}$<3 keV$_{er}$.

The extension of the model to higher energies through the empirical Doke-Birks parameterization [34], in good agreement with data from the ARIS experiment above $\sim$40 keV$_{er}$ [35], is not compatible with ^{39}Ar data in the 3–20 keV$_{er}$ range. Instead, the agreement with ^{39}Ar data

is recovered in the whole data range, as shown in Figure 2, by adding a custom term to Eq. 5, as follows

$$Q_y^{ER} = \left(\frac{1}{\gamma} + p_0 \, (E_{er}/\text{keV}_{er})^{p_1}\right) \frac{\ln(1 + \gamma \, \rho \, E_{er})}{E_{er}}, \quad (6)$$

with two free parameters, p_0 and p_1.

The fit yields C_{box}=9.2±0.9 V/cm, ρ=54.4± 7.3 keV$_{er}^{-1}$, p_0=0.11±0.03, and p_1=1.71±0.08. The C_{box} and ρ parameters are compatible within 1σ with 8.6±1.5 V/cm and 52.7±10.9 keV$_{er}^{-1}$, respectively, obtained from the fit with the Thomas-Imel box model up to 3 keV$_{er}$. It is worth highlighting that the extrapolation of the ER ionization yield below the lowest measured energy (179 eV$_{er}$ from the ^{37}Ar L1-shell electron) is weakly dependent on the custom term introduced in Eq. 6 as it is mainly driven by the Thomas-Imel box model.

To test the impact of the constant excitation-to-ionization ratio assumption, an energy-dependent parametrization was introduced in Eq. 6, so that

$$\rho \to \frac{\rho}{1 + \alpha(E_{er})}, \quad (7)$$

where

$$\alpha(E_{er}) = \frac{0.21}{1 + e^{(E_{er} - b_1)/b_2}}, \quad (8)$$

is a sigmoid function tending to the excitation-to-ionization ratio (N_{ex}/N_i) of 0.21, as measured at high energies [34]. The fit of ^{37}Ar and ^{39}Ar data, assuming the change of variable as in eq. 7, requires two additional free parameters, and does not lead to significant variations of Q_y^{ER} with respect to the constant ρ approximation. Therefore, we conclude that data are not sensitive to either assumption and opt to retain the formalism with constant N_{ex}/N_i that represents the simplest model.

V. NUCLEAR RECOIL IONIZATION YIELD

The NR ionization yield (Q_y^{NR}) is formalized in analogy with the ER one in eq. 3,

$$Q_y^{NR} = \frac{N_{i.e.}}{E_{nr}} = \frac{(1 - r)N_i}{E_{nr}} \quad (9)$$

where the electron recombination probability, r, is described by the Thomas-Imel box model in eq. 4.

Under the assumption that the excitation-to-ionization ratio is constant, N_i can be expressed [36] as:

$$N_i = \beta \, \kappa(\epsilon) \; = \; \beta \, \frac{\epsilon \, s_e(\epsilon)}{s_n(\epsilon) + s_e(\epsilon)} \quad (10)$$

where β is a normalization constant taken as the second free parameter of the model together with C_{box}. The

dimensionless parameter κ represents the energy lost in electronic excitations giving rise to ionization and scintillation signals. s_e is the rate at which electrons are excited by inelastic collisions while s_n is the rate at which energy is transferred to recoiling nuclei by elastic collisions. They all depend on the dimensionless parameter (ϵ) defined as:

$$\epsilon = \frac{a}{2e^2Z^2} \, E_{nr}/\text{keV} \; \simeq \; 0.0135 \, E_{nr}/\text{keV} \quad (11)$$

where the Thomas-Fermi screening length $a = 0.626 \cdot a_0 \cdot Z^{-1/3}$ [36] is used with $a_0 = \hbar/(\alpha m_e c) \simeq 0.529 \cdot 10^5$ fm. The stopping power, s_e, can be expressed as [36]:

$$s_e(\epsilon) = \frac{0.133 \, Z^{2/3}}{A^{1/2}} \, F(v/v_0) \, \sqrt{\epsilon}$$
$$\simeq \; 0.145 \; F(v/v_0) \, \sqrt{\epsilon} \quad (12)$$

where $F(v/v_0)$ is a correction factor dependent on the nuclear (v) and Bohr ($v_0 = e^2/\hbar$) velocities. With no available theoretical calculation backing either a suppression or an enhancement of the electronic stopping power, we assume $F(v/v_0)$=1. However, at the end of this section, we define an ad-hoc function as in Ref. [36] to test the sensitivity of the calibration data to a potential suppression of $s_e(\epsilon)$ at low energies.

The nuclear stopping power, s_n, is modelled by Ziegler et al. using an universal screening function [37]:

$$s_n(\epsilon) = \frac{\ln(1 + 1.1383f_Z \, \epsilon)}{2[f_Z \, \epsilon + 0.01321(f_Z \, \epsilon)^{0.21226} + 0.19593(f_Z \, \epsilon)^{0.5}]} \quad (13)$$

where $f_Z \simeq 0.953$ is a conversion factor for argon that accounts for the slightly different dimensionless energy definition used in Ref. [37] compared to Eq (11).

The NR response model is applied to simulated events analogously to what done for ERs in Section III. The only difference is in the intrinsic resolution of the NR ionization process. Following the procedure used in Ref. [8], we considered two extreme models: one allowing for fluctuations in energy quenching, ionization yield, and recombination processes obtained with binomial distributions, and an other where the fluctuations in energy quenching are set to zero. The analysis described in the below cannot distinguish between the two models, as the difference in the results is negligible. For this reason, in the following, we only consider the model without quenching fluctuations.

The model from Eq. 9 is constrained by fitting DarkSide-50 calibration data, using ^{241}Am-^{13}C and ^{241}Am-^{9}Be neutron sources [38], acquired during the underground argon (UAr) campaign, and external datasets from the SCENE [39], ARIS [35], and Joshi et al. [40] experiments, as described in the following.

FIG. 4. Comparison between AmC spectrum (black) and contamination from TPC intrinsic events and γs from ^{241}Am, as described in the text. The low-energy excess is due nuclear recoils induced by neutrons.
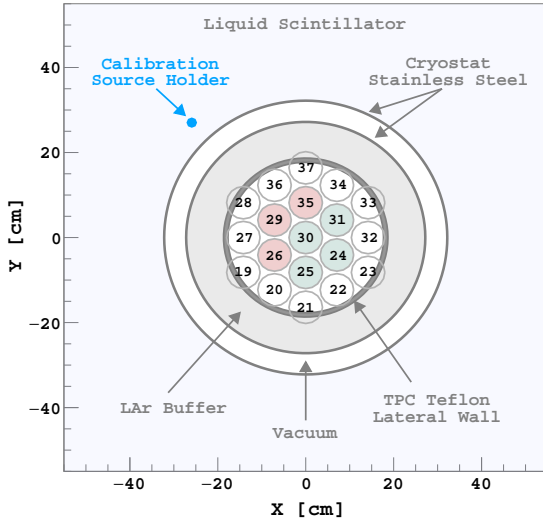
FIG. 3. Schematic top view of the detector. The source holder is located in the liquid scintillator veto. Source events have to cross the cryostat, the LAr buffer and the PTFE walls before reaching the active mass. Events whose position is associated to channels in the outer ring (white) are not included in this analysis. Only events with maximum fraction of light observed by PMTs highlighted in green in the figure are included in the AmC analysis. The analysis of the AmBe source is extended also to events selected by PMTs highlighted in red.

A. ^{241}Am-^{13}C data selection

The ^{241}Am-^{13}C (from now on AmC) neutron source [41] is located outside the DarkSide-50 cryostat, in the liquid scintillator veto, as shown in Figure 3. The source emits neutrons via (α, n) on ^{13}C, producing ^{16}O in the ground level in the final state. First or second excited states, accompanied by γ emission from ^{16}O* de-excitation, are suppressed by a thin degrader, which reduces the α energy below that needed to reach the lowest excited state of ^{16}O.

A 2 mm thick lead shielding absorbs ^{241}Am X-rays, resulting in a neutron source with very low correlation with γ and X emission. However, to compensate for the low efficiency in neutron production, the ^{241}Am activity is rather high (∼3.6 MBq), producing pile-up X-rays and γs with a non-negligible probability of escaping the shielding and reaching the active volume of DarkSide-50, crossing the cryostat, the LAr buffer surrounding the TPC, the field-shaping copper rings, and the PTFE walls housing the active volume.

The ^{241}Am γ-ray with the highest branching ratio (35.9%) has an energy of 59.5 keV that falls in the regime dominated by the photoelectric effect and is fully absorbed in the LAr buffer and preceding materials. ^{241}Am γ-rays with an energy >99 keV and branching ratio
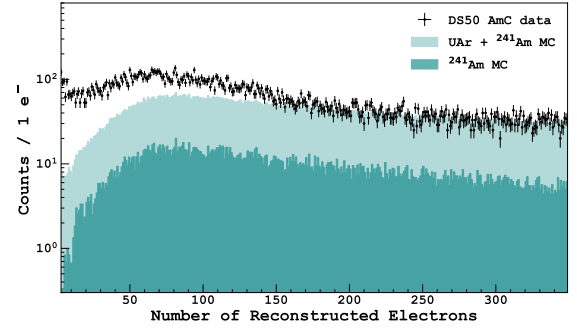
>10^{-9}, as quoted in [42], are simulated with G4DS [18], the DarkSide-50 Monte Carlo, to derive the spectrum of AmC uncorrelated events. The detector response is applied as described in Section III.

The AmC NR analysis is performed on events with Ch_{max} corresponding to channels 24, 25, 30, and 31, the 4 central PMTs less exposed to the source, as shown in Figure 3, with ^{241}Am γ contamination minimized to 5.2%, as estimated from a Monte Carlo simulation. Events selected by channels 26, 29, and 35 (see Figure 3) are excluded from the analysis because of the high rate of ^{241}Am γs. Events not correlated with the source are subtracted using data from the UAr campaign, selected with the same Ch_{max} cuts and normalized by the livetime.

Figure 4 shows AmC and UAr data spectra, the latter normalized by the livetime, and the simulated spectrum of γ-events from ^{241}Am reaching the TPC. The uncertainty on the source position affects the amplitude of the simulated spectrum, which is then normalized to the UAr–subtracted AmC spectrum in the [250, 900] N_e range, where no NR event is expected. The excess of events from the source, shown in Figure 4, with respect to the TPC intrinsic contamination and to simulated ^{241}Am γ-rays, is attributed to neutron scatterings.

B. ^{241}Am-^{9}Be data selection

The ^{241}Am-^{9}Be source (from now on AmBe) emits neutrons in association with the emission of, among others, 4.4 MeV γs. The prompt γ signal is detected in the liquid scintillator veto [17], where the source is deployed. Most neutrons, once scattered in the TPC LAr target, escape the TPC given the low neutron capture cross section in ^{40}Ar. Scattered neutrons that reach the neutron veto are mostly captured by ^{10}B with 22 μs mean time.

NRs in the TPC are selected with a three-fold coincidence by looking at the prompt 4.4 MeV γ, followed by a single-scatter signal in the TPC within a few tens
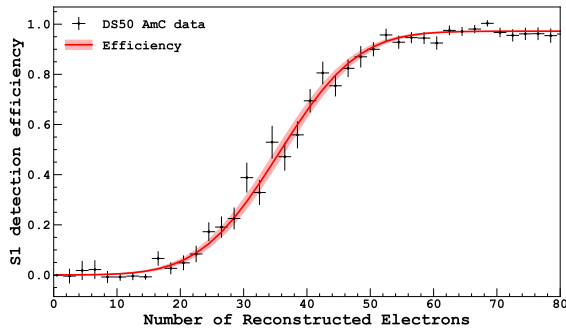
FIG. 5. Efficiency in detecting S1+S2 events (N_{2p}) with respect to S1+S2 and S2-only (N_{1p}), as a function of the reconstructed number of electrons. Data are fitted with an error function (red line). The error band is propagated from the uncertainties of the fitted parameters.
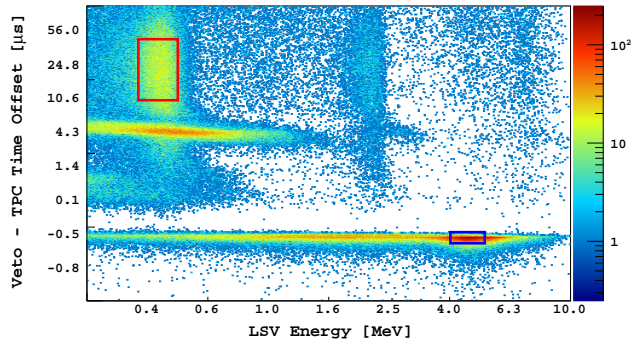

FIG. 6. Veto selection of prompt (blue box) and delayed (red box) events associated to AmBe neutron emission, as a function of liquid scintillator veto (LSV) visible energy and time difference between veto and TPC signals. The trigger time offset between the two detectors is about -550 ns. The horizontal feature at the 4.3 μs offset is due to PMT afterpulses.

of nanoseconds, in turn followed by the delayed neutron capture in the veto. In order to apply this selection, events with both S1 and S2 pulses are required. The events with S2 signal only, in fact, are delayed by the drift time up to a maximum of 376 μs, much longer than the coincidence time with the prompt signal in the veto, which, in most cases, falls outside the acquisition window. On the contrary, the S1 signal is very fast, and allows not to miss the coincidence with the prompt signal in the veto. The requirement of an S1 signal, however, implies an energy threshold, dictated by the S1 trigger and pulse-finder efficiencies. The overall efficiency for NR events is defined as the ratio between 2-pulses events (S1+S2) and all events with either S2-only or S1+S2. The efficiency is extracted from the AmC dataset, by subtracting the ER contamination from each of the two S2-only and S1+S2 samples. The resulting efficiency, which from now on is named S1 detection efficiency, is fitted with an error function, which takes into account Gaussian fluctuations
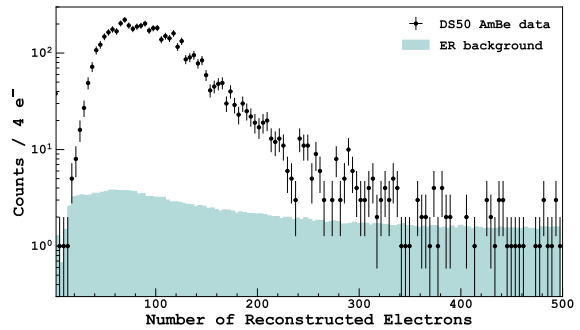

FIG. 7. Spectrum of events selected in triple coincidence (black), compared with accidentals with $f_{90}<0.4$ from the UAr sample, normalized to events selected in the AmBe sample with N_e in the [200, 500] range.

expected in the S1 efficiency, as shown in Figure 5.

Prompt signals in the veto are selected by requiring an electron equivalent energy in the [4, 5] MeV range, and a time difference with respect to the TPC between -600 and -500 ns, taking into account the time offset of -550 ns between veto and TPC. The delayed signal is selected in the [10, 45] μs time window, and with event energy in the [370, 510] keV range, a range properly tuned to account for quenching effects and γ energy deposition in passive materials. The 10 μs low time threshold is applied to avoid veto PMT afterpulses. The selection cuts are shown in Figure 6.

The AmBe events selected in triple coincidence still suffer from a residual contamination due to accidental ERs. Such a contamination is account for by looking in control region where no NR is expected. The control region is defined selecting events with N_e in the [200, 500] range and with $f_{90}<0.4$, where f_{90} is the pulse shape discrimination estimator of DarkSide-50 [15], less than 0.4, a region where no NR is expected. The UAr spectrum is normalized with respect to the same selection criteria, and subtracted from the AmBe one. The contributions from AmBe and non-source events are shown in Figure 7.

C. External datasets

A further constraint to the LAr response to the ionization signal is provided by "external" datasets, i.e. measurements perfomed with small scale LAr detectors exposed to neutron beams. The SCENE collaboration [39] measured the ionization yield for 4 NR energies, between 16.9 and 57.3 keV, with g_2=3.1±0.3 pe/e⁻. The drift field at 193 V/cm is very close to one used in DarkSide-50 (200 V/cm), and the difference is assumed negligible in this analysis. SCENE results are normalized to the DarkSide-50 response by the ratio between the corresponding g_2's.

The ARIS collaboration [35] characterized the LAr scintillation response at 200 V/cm for 8 NR energies, between 7.1 and 117.8 keV. ARIS S1 data at 200 V/cm are rescaled to the DarkSide-50 response by the ratio between field-off S1 yields of DarkSide-50 (8.0±0.1 pe/keV) and ARIS (6.35±0.05 pe/keV). This allows to associate the NR nominal energies from ARIS to the correspondent S1 at 200 V/cm in DarkSide-50. The final step is the conversion of the so-obtained S1 values to S2, by looking at the S2/S1 ratio from NRs selected with the triple coincidence in the AmBe dataset. The correlation between S1 and S2 signals for the AmBe source was accounted for by means of Monte Carlo simulations, which embeds the DarkSide-50 energy and optical response models [18]. The resulting ionization yield is slightly lower at low energies than that published in 2018 [8]. This difference is due to the improved modelling of the detector response.

Joshi *et al.* [40] have measured the ionization yield of NRs at 6.7 keV using the endpoint of a spectrum induced by monochromatic 70 keV neutrons from a beam. The measurement at 240 V/cm, the closest field to the DarkSide-50 one, results in $Q_y=3.6^{+0.5}_{-1.1}$ e$^-$/keV. However, after consulting with the authors, the data point is corrected for their single electron yield using the 2.82 keV K-shell capture ^{37}Ar line from their experiment and DarkSide-50 as a cross-calibration point. The corrected value is then $Q_y=6.0^{+0.8}_{-1.8}$ e$^-$/keV. However, because of this correction, we preferred not to include the measurement by Joshi *et al.* in this analysis, but to quote it in the comparison with the final result.

D. Global fit to data

The energy Monte Carlo spectra for fitting both AmC and AmBe data samples are generated with G4DS, which accurately describes detector and source geometries, with a statistics of about 10^5 neutron events, between 1 and 2 orders of magnitude higher than the data statistics. The detector response is applied with a toy Monte Carlo approach, as described earlier, by varying β and C_{box} parameters from the model with a fine scan. In addition, in order to take into account the inefficiency on S1 pulses, the efficiency curve shown in Figure 5 is applied to AmBe simulated events as a function of N_e.

The AmC and AmBe datasets are simultaneously fitted with a χ^2 analysis in the [3, 250] N_e range. The fit includes g_2 as an additional fit parameter constrained to the measured value within its uncertainty. To minimize the statistical fluctuations, the χ^2 value is averaged over 800 toy simulations for each (β, C_{box}) parameter pair. The resulting χ^2 map in the (β, C_{box}) parameter space is summed to the one from the simultaneous fit of the external datasets from SCENE and ARIS presented in the previous section.

The resulting best parameters of such a global fit are $C_{box}=8.1^{+0.1}_{-0.2}$ V/cm and $\beta=(6.8^{+0.1}_{-0.3})\times10^3$. The corresponding model of the ionization yield is shown as a
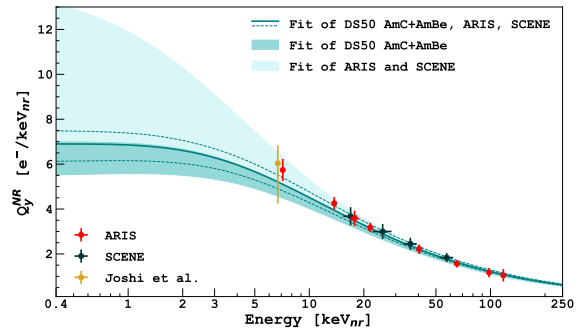

FIG. 8. Fit of the NR ionization yield at 200 V/cm from the combined fit of DarkSide-50 AmBe and AmC calibration data, together with datasets from SCENE [39] and ARIS measurements [35], the latter combined with the DarkSide-50 ionization-to-scintillation ratio. The measured Q_y^{NR} by Joshi *et al.* [40] at 6.7 keV$_{nr}$ is reported for comparison. The model bands correspond to 1 σ uncertainty.

function of the nuclear recoil energy in Figure 8. The errors on the model are from statistical uncertainties and systematic error on g_2. The Q_y^{NR} extracted from external datasets only is in excellent agreement with the one from AmC and AmBe calibrations, as shown in Figure 8, and the reduced χ^2 from combined fit of all the datasets is equal to 1.34 (χ^2/NDF = 676/506). Figure 9 shows the comparison between data and model, for both AmC and AmBe, assuming best fitted parameters. The model is constrained at low energy by the AmC calibration data, with a minimum energy value of 435^{+47}_{-34} eV$_{nr}$, corresponding to 3 electrons. This is the lowest NR calibration threshold ever achieved in LAr.

Regarding potential systematics, we have investigated the impact of S1 detection efficiency on the result for 5 low thresholds, ranging from 0 to 40 N_e, applied to the AmBe dataset. The results obtained by repeating the fit for each threshold are in agreement within 1 σ with the one without threshold, confirming that the S1 detection efficiency does not induce any appreciable systematics.

E. Sensitivity to other theoretical models

We have investigated the sensitivity of our data to different models of the nuclear stopping power as a function of energy stemming from different assumption on screening effects from atomic electrons. This is encapsulated in screening functions arising from different models that can be written as [36]

$$f(\eta) = \frac{\lambda\,\eta^{1-2m}}{\left(1 + \left[2\,\lambda\,\eta^{2(1-m)}\right]^q\right)^{1/q}}, \qquad (14)$$

with each model characterised by a different set of parameters. The additional tested models, as suggested by
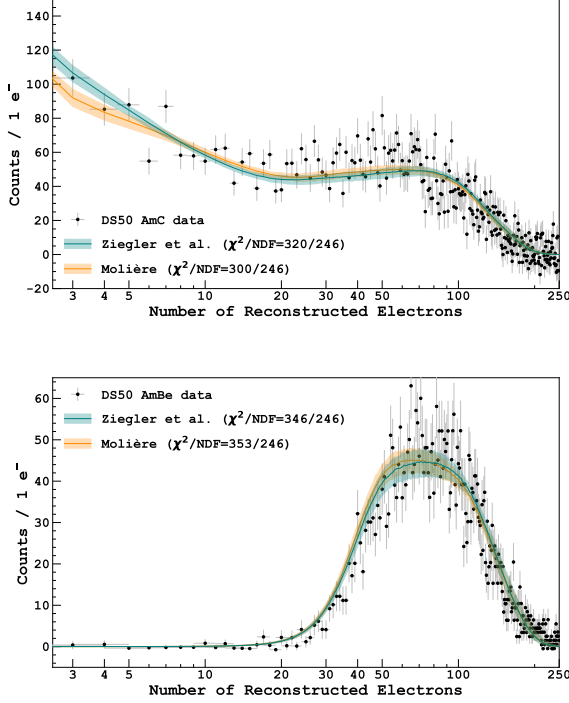
FIG. 9. Best fitted simulated N_e spectra using Ziegler *et al.* (blue) and Molière (orange) screening functions, compared to AmC (top) and AmBe (bottom) data. The model bands correspond to 1σ uncertainty.

Bezrukov *et al.* [36], are Molière ($m = 0.216$, $q = 0.570$, $\lambda = 2.37$) [43], and Lenz-Jensen ($m = 0.191$, $q = 0.512$, $\lambda = 2.92$) [44, 45]. Each of them leads to a different nuclear stopping power through

$$s_n(\epsilon) = \frac{1}{\epsilon} \int_0^\epsilon f(\eta)\, d\eta, \qquad (15)$$

with ϵ from Eq. 11. The Thomas-Fermi screening function, also investigated by Bezrukov *et al.* [36], is not included in this study as it is relevant when the projectile is a naked nucleus or an elementary particle, but not for partially ionized atoms.

The above-described analysis was performed for the Molière and Lenz-Jensen models and was found that both can fit successfully the data, with no statistically significant difference among them. The Q_y^{NR}'s obtained from the fit using the different screening functions are shown in Figure 10. The comparison between model and data for two cases, Ziegler *et al.* and Molière, is shown in Figure 9.

The Ziegler *et al.* model is the one yielding the lowest Q_y^{NR} in the region of interest for WIMP analysis. Therefore the adoption of this model will result in the more conservative choice for the sensitivity to WIMPs in future DarkSide searches.
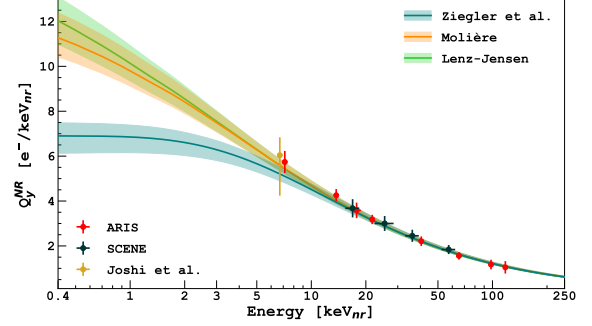
FIG. 10. Fit of DarkSide-50 AmBe and AmC data, and ARIS and SCENE datasets using Ziegler *et al.* (eq. 13) [37], Molière [43], and Lenz-Jensen [44, 45] screening functions. The model bands correspond to 1σ uncertainty.

Following the same conservative approach, we also explored the impact of a low-energy s_e suppression by introducing the functional form of $F(v/v_0)$ in eq. 12 as suggested in [36]:

$$F(v/v_0) = 1/2\ (1 + \tanh(50\ \epsilon - z)), \qquad (16)$$

where $F(v/v_0) \to 1$ for $z \to -\infty$. Setting $z = 0.25$ enables to reproduce the attempt in [46] to include Coulomb effects in the calculation of the electronic stopping power. Such a suppression, demonstrated to be not compatible with existing LXe datasets [36], affects the energy range in LAr below ~ 3 keV$_{nr}$, as shown in Figure 11. Through a null hypothesis test, where the null hypothesis corresponds to $F(v/v_0)=1$, we verified that low energy AmC data have the power to constrain suppression effect to be within $\sim 18\%$ ($2\,\sigma$) at 1 keV$_{nr}$ below the nominal charge yield derived from the universal function. This test allows to exclude $z > 0.04$ or $Q_y^{NR}(1\ \text{keV}_{nr}) < 5.6\ e^-$ / keV$_{nr}$ at 95% C.L..

VI. CONCLUSIONS

In this work, we presented the calibration of the LAr ionization response to electronic and nuclear recoils in the keV region at 200 V/cm with DarkSide-50. The electronic recoil one is measured down to 179 eV$_{er}$, the energy of the L1-shell Auger electron from ^{37}Ar, and extrapolated down to few tens of eV by fitting data with the Thomas-Imel box model. The nuclear recoil ionization response is measured with a low threshold of ~ 500 eV$_{nr}$, corresponding to 3 ionization electrons, the lowest ever performed in LAr. The measured ER and NR ionization yields will impact direct dark matter searches with LAr, extending the observation window to low-mass candidates, like Weakly Interacting Massive Particles of few GeV/c^2 mass, axion-like particles, dark photons and sterile neutrinos, and to neutrino bursts from core-collapse supernovae [47]. Dedicated campaigns of measurement
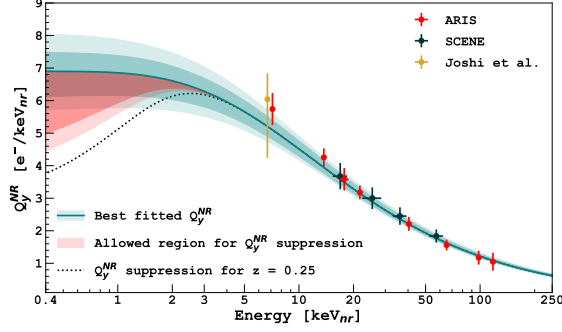
FIG. 11. Allowed region (red) for low energy Q_y^{NR} suppression tested on the AmC dataset, and best fitted Q_y^{NR} (blue), using the Ziegler *et al.* screening function. Dark (light) shaded area corresponds to 1σ (2σ) uncertainty. The dashed line represents the Q_y^{NR} suppression tested in [36] assuming eq. 16 with z=0.25.

with setups exposed to neutron beams are highly desirable in the future to improve and better constrain response models at the keV scale.

ACKNOWLEDGMENTS

[1] E. Aprile *et al.* (XENON), Phys. Rev. Lett. **121**, 111302 (2018), arXiv:1805.12562 [astro-ph.CO].

[2] X. Cui *et al.* (PandaX-II), Phys. Rev. Lett. **119**, 181302 (2017), arXiv:1708.06917 [astro-ph.CO].

[3] D. Akerib *et al.* (LUX), Phys. Rev. Lett. **118**, 021303 (2017), arXiv:1608.07648 [astro-ph.CO].

[4] R. Ajaj *et al.* (DEAP), (2019), arXiv:1902.04048 [astro-ph.CO].

[5] P. Agnes *et al.* (DarkSide), Phys. Rev. **D98**, 102006 (2018), arXiv:1802.07198 [astro-ph.CO].

[6] E. Aprile *et al.* (XENON), Phys. Rev. Lett. **123**, 251801 (2019), arXiv:1907.11485 [hep-ex].

[7] E. Aprile *et al.* (XENON), Phys. Rev. Lett. **123**, 241803 (2019), arXiv:1907.12771 [hep-ex].

[8] P. Agnes *et al.* (DarkSide), Phys. Rev. Lett. **121**, 081307 (2018), arXiv:1802.06994 [astro-ph.HE].

[9] P. Agnes *et al.* (DarkSide), Phys. Rev. Lett. **121**, 111303 (2018), arXiv:1802.06998 [astro-ph.CO].

[10] P. Sorensen *et al.* (XENON10), Nucl. Instrum. Meth. A **601**, 339 (2009), arXiv:0807.0459 [astro-ph].

[11] L. Goetzke, E. Aprile, M. Anthony, G. Plante, and M. Weber, Phys. Rev. D **96**, 103007 (2017), arXiv:1611.10322 [astro-ph.IM].

[12] D. Akerib *et al.* (LUX), (2016), arXiv:1608.05381 [physics.ins-det].

[13] E. Aprile *et al.* (XENON), Phys. Rev. D **97**, 092007 (2018), arXiv:1709.10149 [astro-ph.IM].

[14] E. Aprile *et al.* (XENON), Phys. Rev. D **99**, 112009 (2019), arXiv:1902.11297 [physics.ins-det].

[15] P. Agnes *et al.* (DarkSide), Phys. Lett. **B743**, 456 (2015), arXiv:1410.0653 [astro-ph.CO].

[16] P. Agnes *et al.* (DarkSide), Phys. Rev. **D93**, 081101 (2016), [Addendum: Phys. Rev.D95,no.6,069901(2017)], arXiv:1510.00702 [astro-ph.CO].

[17] P. Agnes *et al.* (DarkSide), JINST **11** (03), P03016, arXiv:1512.07896 [physics.ins-det].

[18] P. Agnes *et al.* (DarkSide), JINST **12** (10), P10015, arXiv:1707.05630 [physics.ins-det].

[19] M.-M. Bé, V. Chisté, C. Dulieu, X. Mougeot, V. Chechev, F. Kondev, A. Nichols, X. Huang, and B. Wang, *Table of Radionuclides*, Monographie BIPM-5, Vol. 7 (Bureau International des Poids et Mesures, Pavillon de Breteuil, F-92310 Sèvres, France, 2013).

[20] X. Mougeot, Appl. Radiat. Isot. **134**, 225 (2018).

[21] X. Mougeot, Applied Radiation and Isotopes **154**, 108884 (2019).

[22] M. Wang, W. Huang, F. Kondev, G. Audi, and S. Naimi, Chinese Physics C **45**, 030003 (2021).

[23] D. E. Cullen, *Program RELAX: A code designed to calculate atomic relaxation spectra of x-rays and electrons*, Tech. Rep. UCRL-ID.110438 1992 (Lawrence Livermore National Laboratory).

[24] D. E. Cullen, *A Survey of Atomic Binding Energies for Use in EPICS2017*, Tech. Rep. IAEA-NDS-0224 (IAEA, 2017).

[25] U. Fano, Phys. Rev. **72**, 26 (1947).

[26] A. G. Santos-Ocampo and D. C. Conway, Phys. Rev. **120**, 2196 (1960).

[27] P. W. Dougan, K. W. D. Ledingham, and R. W. P. Drever, The Philosophical Magazine: A Journal of Theoretical Experimental and Applied Physics **7**, 475 (1962).

[28] D. Totzek and K. W. Hoffmann, Zeitschrift für Physik **205**, 137 (1967).

[29] T. Doke, A. Hitachi, S. Kubota, A. Nakamoto, and T. Takahashi, Nuclear Instruments and Methods **134**, 353 (1976).

[30] J. Thomas and D. A. Imel, Phys. Rev. A **36**, 614 (1987).

[31] M. Jaskolski and M. Wojcik, J. Phys. Chem. A **115**, 4317 (2011).

[32] T. Doke, A. Hitachi, J. Kikuchi, K. Masuda, H. Okada, and E. Shibamura, Jap. J. Appl. Phys. **41**, 1538 (2002).

[33] P. Sorensen and C. E. Dahl, Phys. Rev. D **83**, 063501 (2011), arXiv:1101.6080 [astro-ph.IM].

[34] T. Doke, H. Crawford, A. Hitachi, J. Kikuchi, P. Lindstrom, K. Masuda, E. Shibamura, and T. Takahashi, Nucl. Instrum. Meth. A **269**, 291 (1988).

[35] P. Agnes *et al.*, Phys. Rev. **D97**, 112005 (2018), arXiv:1801.06653 [physics.ins-det].

[36] F. Bezrukov, F. Kahlhoefer, and M. Lindner, Astropart. Phys. **35**, 119 (2011), arXiv:1011.3990 [astro-ph.IM].

[37] J. P. Biersack and J. F. Ziegler, in *Ion Implantation Techniques*, edited by H. Ryssel and H. Glawischnig (Springer Berlin Heidelberg, Berlin, Heidelberg, 1982) pp. 122–156.

[38] P. Agnes *et al.* (DarkSide), JINST **12** (12), T12004, arXiv:1611.02750 [physics.ins-det].

[39] H. Cao *et al.* (SCENE), Phys. Rev. **D91**, 092007 (2015), arXiv:1406.4825 [physics.ins-det].

[40] T. H. Joshi *et al.*, Phys. Rev. Lett. **112**, 171303 (2014), arXiv:1402.2037 [physics.ins-det].

[41] J. Liu, R. Carr, D. A. Dwyer, W. Q. Gu, G. S. Li, R. D. McKeown, X. Qian, R. H. M. Tsang, F. F. Wu, and C. Zhang, Nucl. Instrum. Meth. **A797**, 260 (2015), arXiv:1504.07911 [physics.ins-det].

[42] R. B. Firestone, C. Baglin, and S. Y. F. Chu, *Table of isotopes: 1996 CD ROM Edition* (Wiley, New York, NY, 1996).

[43] G. Moliere, Zeitschrift fr Naturforschung A **2**, 133 (1947).

[44] W. Lenz, Zeitschrift fr Physik **77**, 713 (1932).

[45] H. Jensen, Zeitschrift fr Physik **77**, 722 (1932).

[46] I. S. Tilinin, Phys. Rev. A **51**, 3058 (1995).

[47] P. Agnes *et al.* (DarkSide 20k), JCAP **03**, 043, arXiv:2011.07819 [astro-ph.HE].